JAAS

The role of ambient gas confinement, plasma chemistry, and focusing conditions on emission features of femtosecond laser-produced plasmas

Journal:	*Journal of Analytical Atomic Spectrometry*
Manuscript ID	JA-ART-03-2020-000111.R1
Article Type:	Paper
Date Submitted by the Author:	26-Apr-2020
Complete List of Authors:	Kautz, Elizabeth; Pacific Northwest National Laboratory, National Security Directorate Yeak, Jeremy; Opticslah Bernacki, Bruce; Pacific Northwest National Lab, Phillips, Mark; University of Arizona, Optics Science Center; Opticslah Harilal, Sivanandan; Pacific Northwest National Laboratory, National Security Directorate

Table of Contents Entry for:

The role of ambient gas confinement, plasma chemistry, and focusing conditions on emission features of femtosecond laser-produced plasmas

Elizabeth J. Kautz, Jeremy Yeak, Bruce E. Bernacki, Mark C. Phillips, and Sivanandan S. Harilal

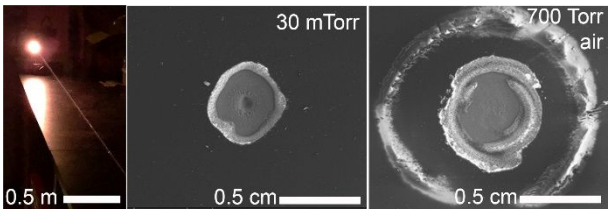

caption: image of the filament ablation with femtosecond laser and filament ablation craters

ARTICLE

The role of ambient gas confinement, plasma chemistry, and focusing conditions on emission features of femtosecond laser-produced plasmas

Received 00th January 20xx,
Accepted 00th January 20xx

DOI: 10.1039/x0xx00000x

Elizabeth J. Kautz,[a] Jeremy Yeak,[b] Bruce E. Bernacki,[a] Mark C. Phillips,[b,c] and Sivanandan S. Harilal[a]*

Ultrafast laser ablation coupled with optical emission spectroscopy is currently under development for standoff detection of elements and their isotopes for a wide range of application areas. In this work, we explore the role of ambient air pressure during the interaction of an ultrafast laser beam with two metallic targets (brass and uranium) with significantly different oxygen gas-phase reactivity. Plasma plumes were generated by focusing ~800 nm, ~35 fs pulses from an ultrafast laser system using a long focal length lens (f = 1 m). Two-dimensional spectral imaging was performed over the pressure range of 30 mTorr-700 Torr air to evaluate emission dynamics, plasma chemistry, signal-to-background ratio, and characteristic parameters (*i.e.* excitation temperature, electron density). An increase in ambient air pressure during ultrafast laser ablation leads to plume confinement and subsequent changes in the emission dynamics due to plasma chemistry as well as changes in plasma generation conditions (*i.e.* focused fs laser ablation *versus* filament ablation). Ablation crater morphologies were also investigated via scanning electron microscopy. Results indicate atomic emission intensity and signal-to-background ratios peak at moderate pressure levels (~50-100 Torr air) for both targets studied, although plasma chemistry influences uranium emission signatures. The emission features of the uranium plasma at pressures ≥ 10 Torr showed the presence of oxide molecules. We also find filament ablation leads to wider, more shallow craters compared to focused laser ablation. Our study provides unique insight into the interplay between plume dynamics, confinement, and plasma chemistry of fs laser-produced plasmas and how these phenomena evolve with changing ambient air pressure.

Introduction

Laser ablation (LA) coupled with optical emission spectroscopy (OES) (commonly referred to as laser-induced breakdown spectroscopy or LIBS) is a technology capable of analysis and detection of elements and their isotopes both in laboratory settings, and at standoff distances.[1] Standoff sensing via LIBS has widespread application in several fields, including geochronology and geologic material sensing, environmental monitoring, cultural heritage diagnostics, on-line process monitoring, and detection of actinides for nuclear safeguards, security, and treaty verification.[2-5] Although LIBS is a well-established and routinely used technique, significant challenges remain in the development of LIBS for elemental and isotopic detection at standoff distances. Some of the challenges include the delivery of sufficient laser energy required for target ablation, and the generation of a bright emitting plasma to allow for the collection of adequate light. To address such challenges, improved understanding of laser and filament produced plasma generation physics at standoff distances, and plume characteristics (including emission properties) is needed.[1, 6-17]

It is well known that laser-produced plasma (LPP) emission signatures depend on a variety of factors, including laser energy, wavelength, pulse width, spot size, target material properties, and environmental conditions.[1, 18, 19] Among these factors, the nature and pressure of the ambient medium (*i.e.* environmental conditions) and laser pulse width may have a profound impact on plume fundamentals as well as the emission persistence.[1, 20] Differences in physics involved during long (ns) and ultrashort (fs) laser-matter interaction can be understood by comparing the duration of the laser pulse to characteristic timescales, such as electron-to-ion energy transfer, electron-heat conduction, and plasma expansion times. All of these phenomena occur on the order of several picoseconds after the onset of ultrafast laser ablation.[1] There exist several reports (including reviews) that cover the fundamental differences between long and short pulse duration laser ablation which highlight the reduced continuum emission, generation of an 'atomic' plume, cleaner craters, generation of lower-temperature plasmas, and reduced matrix effects for fs LPP in comparison to ns LPP.[1, 2, 4, 21]

The interaction of an ultrafast laser with ambient gas at varying pressures is complex, considering the nonlinear interaction of an ultrafast laser beam with a transparent medium such as air.[13] Ultrafast laser pulses in transparent media (air for example) can undergo self-focusing due to the non-linear Kerr effect, leading to the formation of plasma channels. Self-focusing of an ultrafast laser pulse requires laser power greater than the peak critical power for self-focusing, $P_{Cr} = 3.72\lambda_0^2(8\pi n_0 n_2)$, where λ_0 is the laser wavelength, n_0 is the linear refractive index, and n_2 is the nonlinear Kerr refractive index.[13, 22] The generated plasma will act as a negative refractive index medium and defocuses the incoming beam. The balance

[a] Pacific Northwest National Laboratory, Richland, WA 99352 USA
[b] Opticslah, LLC, Albuquerque, NM 87106, USA
[c] James C. Wyant College of Optical Sciences, University of Arizona Tucson, AZ 85721, USA
*Corresponding Author: hari@pnnl.gov

between self-focusing and defocusing of the ultrafast laser beam leads to the formation of filaments. Filaments generated by ultrafast laser pulses typically contain ~10% of the laser energy and the remaining energy will be deposited in a photon bath or energy reservoir around the filament. Due to the unique ability of ultrafast lasers to self-focus in air and thus propagate to large distances (hundreds to thousands of meters[12, 14, 23]), there is significant interest in their application for standoff detection of elements and their isotopes, aerosols, and atmospheric gases.[13, 21] Reported filament peak intensity of ~5×10^{13} Wcm^{-2} is sufficient for ablating any solid target material.[13] However, further study is required to understand the emission signatures of filament produced plasmas and how they vary with ambient pressure conditions.

The nature and pressure of the ambient gas medium and associated plume chemistry can greatly impact laser-target interaction, expansion dynamics, and characteristic parameters of the plasma plume.[24-26] The role of pressure of ambient environment on plasma expansion dynamics, as well as emission features, for both ns and fs LPPs have previously been studied.[20, 27] The change in air pressure from vacuum, and moderate pressure levels, to atmospheric pressure conditions transforms the ablation from focused fs to filament ablation. With increasing pressure, emission intensity is expected to be enhanced due to increased plume-ambient collisions and confinement. When the mean free path of ambient species becomes greater than the characteristic Debye length of the LPP, the expanding plasma experiences phenomena such as gas-plasma collisional interactions, plume morphological changes (*e.g.* splitting, sharpening), and confinement.[28] The presence of plasma chemistry may also influence the absorption and emission persistence by oxidizing the plume species if the target is pyrophoric.[28, 29] All of these factors affect analytical figures of merit (*e.g.* signal-to-noise and signal to background ratios), emission signatures, plume properties, and ablation efficiency in ultrafast laser and filament LIBS.

Although numerous research articles are available about the LIBS plume fundamentals[30], ambient gas effects[31], focusing conditions on plume morphology[32], and ns *versus* fs LIBS comparison[1, 4, 5], limited studies exist on plasma chemistry, or more specifically, gas-phase oxidation and its influence on emission features, plume persistence, and plume fundamentals. Recently, significant modelling and experimental efforts have been dedicated to understand U plasma chemistry.[24, 26, 28, 33-35] Laser produced U plasmas oxidize rapidly in a high-temperature, oxygen-containing environment, forming UO and polyatomic oxide molecules (U_xO_y).[24, 33, 36] Finko *et al.*[25, 26] documented some of the most favourable thermochemistry and plasma chemistry reaction pathways for the formation of U_xO_y. Emission spectroscopic analysis in conjunction with optical modelling of U spectral features demonstrated the optimal temperature range for UO formation is ~1500–5000 K.[18] A monochromatic imaging study employing narrowband filters for U I and UO emission showed UO species are primarily formed further from the target (in comparison to U atoms), where lower temperatures favour molecular recombination.[33] In addition to these studies, several emission and absorption based studies have focused on identifying various emission bands of UO, UO_2, and U_xO_y.[37-39]

Both atomic and molecular emission can be utilized for the detection and analysis of elements and isotopes.[1, 40, 41] However, the impact of ambient gas chemistry and pressure on atomic and molecular emission signatures is not as well characterized for ultrafast (*i.e.* fs) LPPs in comparison to ns LPPs. It is documented that ultrafast LA produces a cooler plasma primarily comprised of atomic species, which is favourable for molecular formation at early times after plasma onset.[42, 43] In this study, we investigate the interrelated roles of plume confinement, chemistry, and focusing conditions of emission features of fs LPPs as a function of air pressure. Plasma expansion, chemistry, emission line intensity, and properties (*i.e* excitation temperature and electron density) were studied, and analysis of crater morphology was performed over a range of ambient air pressure levels (30 mTorr – 700 Torr) for a constant laser energy of ~6 mJ. We used a long focal length lens (f = 1 m) for generating plasmas from two metal targets with varying pyrophoricity (U and brass). The change in air pressure from low/moderate pressure levels to near atmospheric conditions transformed the ablation mechanism from focused fs LA to filament LA, where plasma chemistry for U plumes was a major factor. 2D spectral imaging was used to compare the plasma expansion and spatially resolved chemistry of U and brass plasmas. Spectral information from brass plasmas was also used to measure the excitation temperature and electron density as a function of pressure. Additionally, imaging via scanning electron microscopy of brass ablation craters was performed to investigate crater morphologies from focused fs and filament ablation conditions. Our study has broad implications to the development of LIBS for sensing of elements and isotopes.

Experimental Details

Pulses from an amplified ultrafast laser system (Ti:Sapphire, Model: Coherent Astrella) providing ~ 800 nm wavelength, ~35 fs full width half maximum (FWHM) operated at 10 Hz with a laser pulse energy of 6 mJ was used for the present study. A f=1 m lens with an anti-reflection coating was used for laser focusing and generating filaments in air. Using these optics, filaments were formed approximately ~93 cm from the focusing lens in near atmosphere conditions (700 Torr air). The experimental set-up used in this work is schematically shown in Figure 1. Target materials used for ablation were brass (Cu-Zn alloy), and natural metallic U metal (0.7% ^{235}U and 99.3% ^{238}U). Targets were fixed in a cubic vacuum chamber (0.125 ft^3 volume) for all experimentation. The chamber was attached to a dry scroll pump and a gas manifold for pressure and ambient gas control. Pressures in the range of 30 mTorr – 700 Torr air were used. The vacuum chamber was equipped with optical windows for laser entrance and light collection, and pressure gauges to allow for monitoring chamber pressure. For avoiding filament induced optical damage to the laser entrance window, a ~70 cm vacuum nipple was attached to the chamber, where the front window of the vacuum nipple was ~78 cm away from

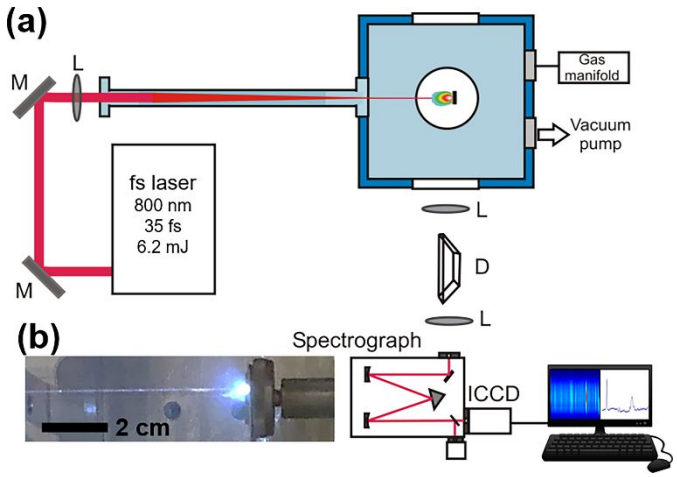

Fig 1 (a) Schematic of the experimental set-up used for collecting spectral features (2D spectral images and spatially integrated spectra), and (b) photograph of filament produced in the vacuum chamber in air. Acronyms used above are: M – mirror, L – lens, D – dove prism, ICCD – intensified charged coupled device.

the target position. The vacuum chamber was fixed to an *x-y-z* translator stage so that the target could be repositioned to prevent target drilling.

An optical system consisting of two plano-convex lenses was used for imaging the plasma plume onto the slit of a 0.5m Czerny-Turner spectrograph (Acton Spectrapro 2500i). The LIBS plume was imaged in such a way that the plume expansion direction was parallel to the slit height with the help of a Dove prism. [44, 45] The spectrograph was coupled to an intensified charged coupled device (ICCD) camera (PIMAX4, 1024 × 1024 pixels) for recording time-resolved and time-integrated 2D spectral images. The spectrograph and ICCD were positioned orthogonal to the plasma expansion direction. Holographic gratings (2400 grooves/mm) optimized for the visible spectral regime were used for recording 2D spatially-resolved, wavelength dispersed images. For recording broad spectral features of brass plasma in the visible spectral region (400-650 nm), the 300 grooves/mm grating was used. For all time-resolved measurements, the ICCD was synchronized with laser pulsing via a programmable timing generator. Additionally, a Thermo Scientific Quanta dual beam focused ion beam/scanning electron microscope (FIB/SEM) was utilized for imaging crater morphologies using the secondary electron detector.

Results

The presence of an ambient gas during ultrafast laser beam transport may lead to the generation of filaments in the beam path. Filaments are formed when the power of the ultrafast laser is greater than the critical power required for self-focusing (P_{cr}).[13] For the 800 nm laser wavelength used in this work, P_{cr} is ~3 GW. In this study, we use peak power of approximately 60×P_{cr}. An increase in ambient air pressure during ultrafast LA may lead to changes in plume emission due to transformation in focusing conditions (filament *versus* focused), confinement, and plasma chemistry (if present). Prior work employing ns laser ablation showed that a change in nature and the pressure of the ambient environment can lead to significant changes in plume emission intensity and properties.[20] Here, we evaluated the emission features of fs laser/filament ablation of two different target materials (brass and U) at various pressure levels. It is well documented that U atoms in an oxygen-containing environment will oxidize rapidly.[24, 33, 36] Thus, spectral features of a U plasma in the presence of an oxygen-containing environment may contain emission from U atoms and ions in addition to U oxide molecules (U_xO_y). The brass target analytes (Cu and Zn) in comparison to U are less susceptible to oxidation. Although CuO has several bands in the visible region, we haven't observed any of these in our system. To the authors' best knowledge, there exist no reports on ZnO emission spectrum from LPPs, and according to Gaydon and Pearse[46] ZnO does not readily give a good band spectrum. Thus, plasma chemistry for the brass plasmas was not observed in our work.

The spectral regions selected for this study are 591-595 nm and 508-524 nm for U and brass plasmas, respectively, and examples of emission spectral features are given in Figure 2. The spectrum from U plasma in this region (sub-figure a) contains emission from U atoms (U I) and U oxide molecular species (e.g. UO, U_xO_y). The major UO feature (molecular band) appears around 593.55 nm. The prominent U I emission lines are a resonance transition at 591.54 nm (0–16900 cm^{-1}) and a near-resonance line at 593.38 nm (620–17468 cm^{-1}). The other U I lines are also marked in Figure 2 and include: 592.55 nm (7646–24 517 cm^{-1}), 592.93 nm (3801–20 662 cm^{-1}), 594.28 nm (5762–22 585 cm^{-1}), and 594.86 nm (7646–24 452 cm^{-1}).[47] In addition to U I and UO transitions, a strong background emission contributed by polyatomic oxides (U_xO_y)[36] is evident in the spectral features from the U plasma. For the brass plasma, the prominent lines in the spectral region are Cu I transitions at 510.55 nm (11203-30784 cm^{-1}), 515.32 nm (40535-49935 cm^{-1}) and 521.82 nm (30784-49942 cm^{-1}). The background emission contributed by molecular species is not apparent in the brass spectrum.

2D spectral images provide emission features of various constituents from the plasma with high spatial resolution and hence are well-suited for tracking plasma oxidation. 2D spectral images of brass and U plasmas at various pressures ranging from 30 mTorr to 700 Torr (~1 atm) air are presented in Figure 3. The delay and integration times used for recording 2D spectral imaging are 1 μs and 20 μs, respectively. The spatial resolution available in the 2D spectral images is dictated by the ICCD pixel size and magnification, and the slit width for y and x axes, respectively. By increasing the ambient air pressure during ultrafast laser-target interaction, the generation mechanism of the plasma will be transformed from focused fs LA to filament ablation. Further, the role of plasma chemistry will be negligible at reduced pressures due to the reduced oxygen number density in the ambient medium. Hence, the 2D spectral imaging of the U and brass plasmas with varying air pressures provide useful information related to plasma-ambient gas interaction, including the changes in the oxidation of the plasma (if present),

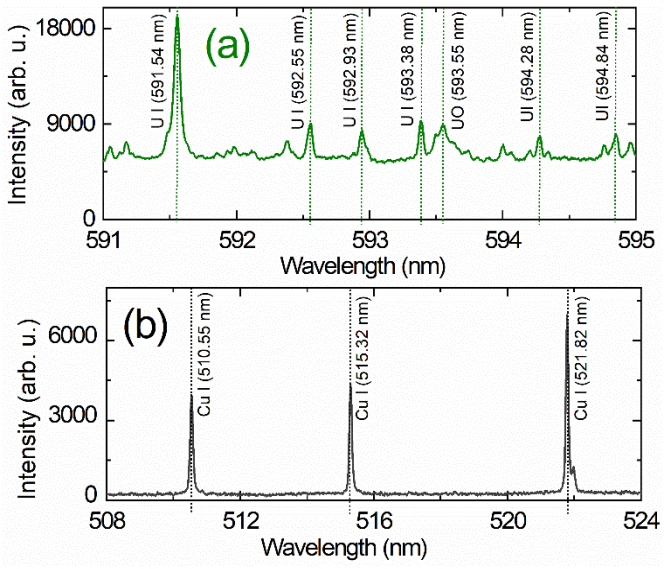

Fig. 2 Spectral emission features from (a) U and (b) brass plasmas in 200 Torr air at a distance of 2 mm from the targets. The emission spectra were collected with a gate delay of 1 μs and an integration time of 20 μs. All intensities are averaged over a 0.2 mm width area centred at 2 mm from the target. Each spectrum represents an average of 15 shots.

confinement, and emission changes due to transformation from focused laser to filament produced plasma.

At low-pressure levels (~30 mTorr), the emission intensity is measurable at distances far away from the target and exceeds the detector's field of view for both U and brass plasmas, indicating free expansion. As pressure is increased, emission from the plasma is confined and this effect is most clearly seen at relatively high ambient pressure levels (≥ 100 Torr). The reduction in plume length is also evident in 2D spectral images. For example, the length of the brass plume decreases from ~5 mm to ~2 mm when the pressure is increased from 100 Torr to 700 Torr air. Similarly, for the U plasma, the plume length is reduced from ~5 mm at 100 Torr to ~3 mm at 700 Torr. Although similar gate times and delays were used for measuring the spectral images of both brass and U plasmas, it is clear that at lower pressures the Cu species moved farther away from the target with negligible emission close to the target. This result can be related to the higher velocities of Cu species compared to U, given the expansion velocities of the species are inversely proportional to the square of the atomic mass.[48] A broadband-like emission is also apparent closer to the target at low-pressure levels for the U plasma. As pressure increases to ~10 Torr, the emission from all species become stronger. For U plasmas, the UO emission ~593.55 nm is also apparent at ~10 Torr, although weaker compared to atomic transitions. At pressure levels > 10 Torr, U I and UO emission is enhanced. With increasing pressure, particularly ≥ 100 Torr, the broadband-like emission from U_xO_y becomes more intense relative to emission from U I and UO, and at 700 Torr the emission from U_xO_y predominates.

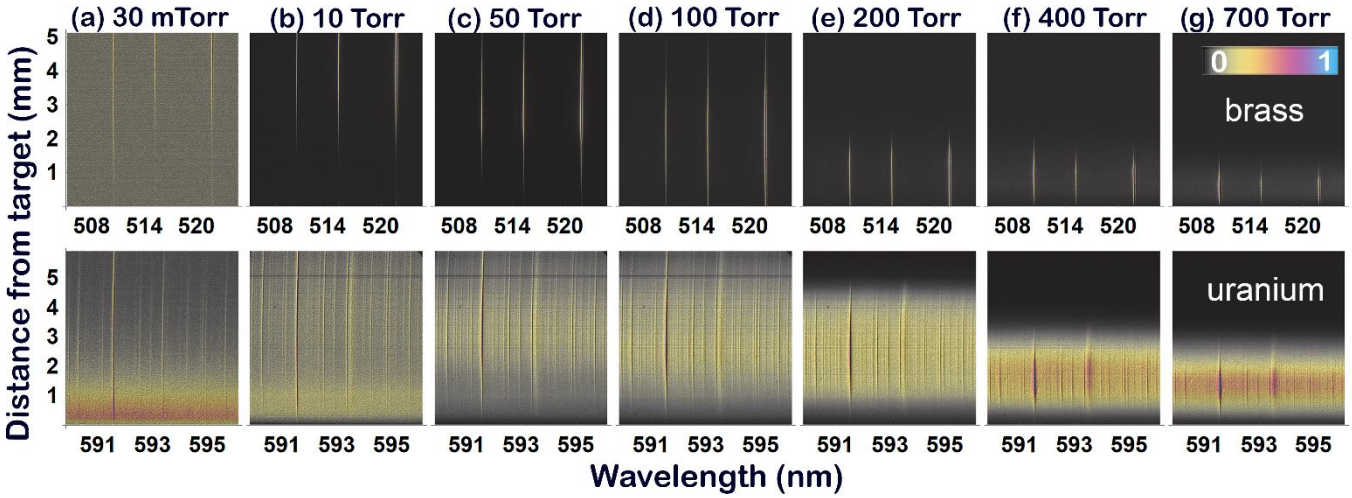

Fig. 3 2D spectral images of laser-produced plasmas from brass (top row) and metallic U (bottom row) target materials at the following pressure levels: (a) 30 mTorr, (b) 10 Torr, (c) 50 Torr, (d) 100 Torr, (e) 200 Torr, (f) 400 Torr, (g) 700 Torr. A false-color map was applied to each spectral image, which was normalized to its maximum intensity. Each image represents the accumulation of 15 shots and is time-integrated over the gate width of 1-21 μs after plasma onset.

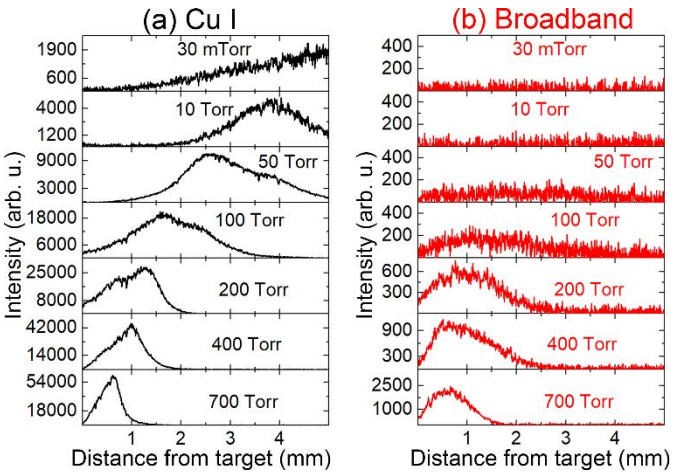

Fig. 4 Intensity versus distance at varying pressures (30 mTorr – 700 Torr) for (a) Cu I (510.55 nm), and (b) broadband. Intensity-distance profiles were calculated from time-integrated spectra from 1-21μs averaged over 15 shots. Intensity-distance profiles represent the intensity averaged over a 0.06 mm width window for broadband and a 0.03 mm width window for Cu I. The wavelength range used for broadband-like emission was 512.50-512.56 nm where no strong atomic or molecular peaks are observed.

2D spectral images (Figure 3) also show a spatial intensity variation between atomic, molecular, and broadband emission features. Hence, intensity-distance contour plots were generated along the expansion direction. Plots presented in Figure 4(a)-(b) show Cu I (510.55 nm) and broadband emission (512.50-512.56 nm) intensities, respectively, as a function of distance from the target for various pressure levels studied. We find Cu I emission increases with increasing background pressure and the maximum intensity region moves towards the target with increasing pressure. Relative to line emission, broadband emission is found to be negligible for the brass plasma at pressures ≤ 10 Torr, and increases marginally for 50-100 Torr. The broadband emission from brass plasma is seen only at closer distances to the target (≤ 2mm) regardless of the ambient pressure, which we attribute to emission from nanoparticles.[49]

While the changes in Cu I emission intensity clearly show confinement effects with increasing ambient pressure, the role of plasma chemistry is negligible. However, for the U analyte, both confinement and plasma chemistry influence the intensity of spectral lines shown in the Figure 3 spectral images. For the U target, the added effect of plasma chemistry allows us to study the expansion and formation dynamics of oxide molecules, in addition to atomic emission features. Thus, we also evaluated intensity-distance changes in U plasmas with varying pressure along the plasma expansion direction, with results given in Figure 5. Figure 5(a),(b),and (c) present contour plots for U I (591.54 nm), UO (593.55 nm) and broadband (593.10-593.16 nm) emission intensities. UO emission is nearly non-existent at 30 mTorr where no oxygen is available for initiating plume chemistry. At 10 Torr, UO signal is stronger farther from the target but is still relatively weak in comparison to U I. For pressures ≥10 Torr to 700 Torr, U I and UO are co-located in the plume over the integration time of 1-21 μs after plasma onset. The broadband emission variation with pressure shows a different spatial evolution, with emission intensity initially close to the target, then with increasing pressure, broadband emission intensity follows a similar trend to UO.

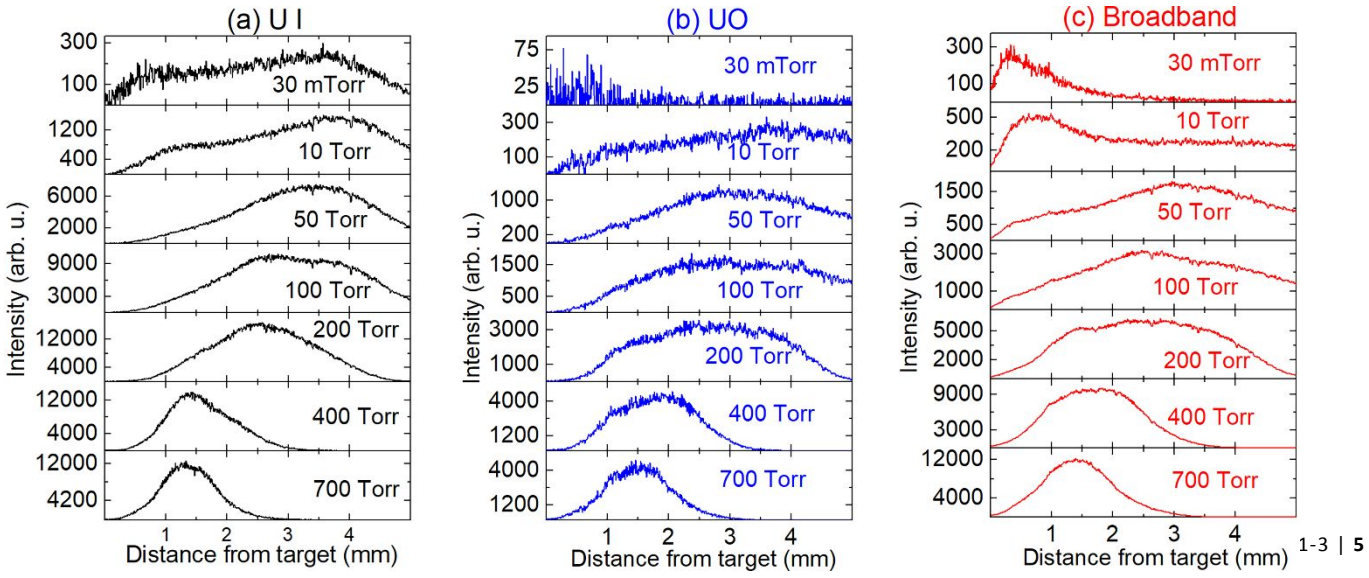

Fig. 5 Intensity versus distance at varying pressures (30 mTorr – 700 Torr) for: (a) U I (591.54 nm), (b) UO (593.55 nm), and (c) broadband. Intensity-distance profiles were calculated from time-integrated spectra from 1-21μs averaged over 15 shots. Intensity-distance profiles represent the intensity averaged over a 0.06 mm width window for UO and broadband and a 0.03 mm width window for U I. The wavelength range used for broadband-like emission was 593.10-593.16 where no strong atomic peaks are observed.

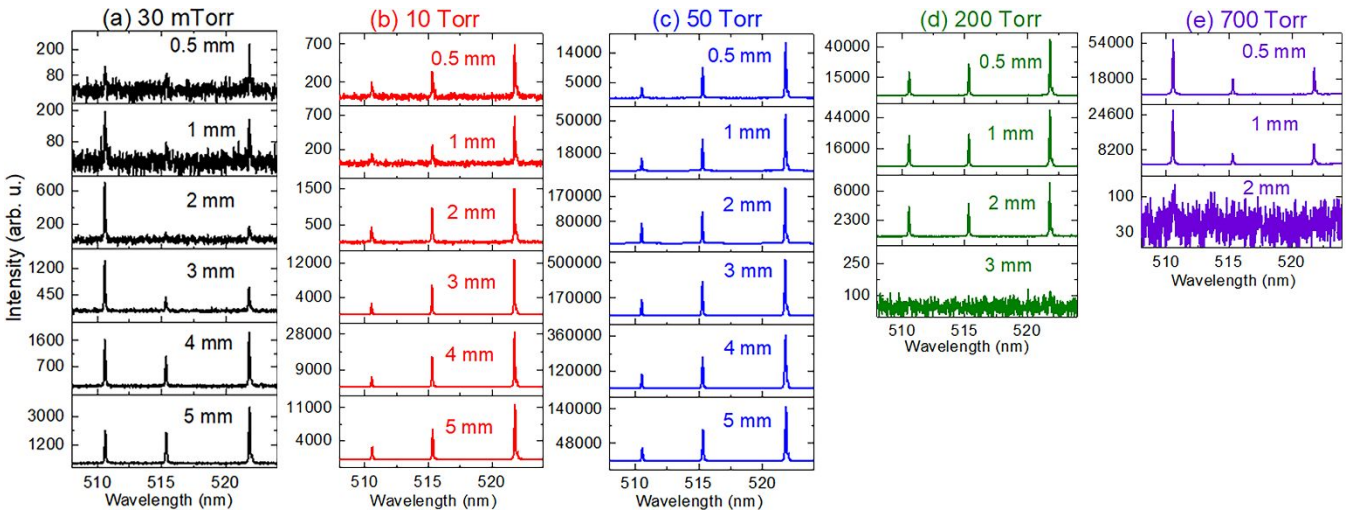

Fig. 6 Time-integrated, spatially-resolved spectral features of brass plasma in the 508-524 nm wavelength range at the following pressure levels: (a) 30 mTorr, (b) 10 Torr, (c) 50 Torr, (d) 200 Torr, and (e) 700 Torr. All spectra are averaged over 15 shots, and intensities are averaged over a 0.2 mm width area. The gate delay and width used for this measurement were 1 μs and 20 μs, respectively. Spectral lines shown in the above spectra correspond to Cu I lines at: 510.55 nm, 515.32 nm, and 521.82 nm.

Spectral images and contour plots presented in Figures 3-5 show significant changes in the emission intensity from plasma species (e.g. Cu I, U I, UO, broadband) with increasing air pressure. To investigate variation in plasma chemistry within the plume, brass and U spectra at varying distances from the target for select pressure levels (30 mTorr, 10 Torr, 50 Torr, 200 Torr, and 700 Torr) were analysed and are given in Figures 6-7. Cu I atomic emission lines show intensity changes with distance for various ambient pressure levels which is more apparent at a lower pressure (30 mTorr). This trend can be correlated to a larger plasma temperature gradient with increasing distance from the target due to free expansion. However, the changes in the intensity of various Cu peaks with distance become less noticeable (except at plume edges) at higher pressure (≥50 Torr), which can be related to thermalization of the plasma due to plume confinement.[50] As pressure is increased to 200-700 Torr, measurable Cu I emission intensity is limited to ~2 mm and ~1 mm from the target for 200 and 700 Torr, respectively, due to plasma confinement at these higher pressure levels.

For the U target, we find that at lower pressures (~30 mTorr), the emission is dominated by U atoms regardless of spatial location within the plasma. The resonance U I transition at 591.54 nm and near-resonance U transition at 593.38 nm are the strongest atomic lines in the spectral region studied (591-595 nm) at all distances from the target. As pressure is increased above 30 mTorr, emission intensity of the UO molecular band at 593.55 nm increases. Similar to the brass analyte, at increasing pressure plume confinement is observed. For the U plasma, the emission signal at 700 Torr is limited to ~3 mm from the target due to confinement effects.

2D spectral images, intensity-distance profiles, and spectral features presented in Figures 3-7 show significant changes in the emission intensity from plasma species (e.g. Cu I, U I, UO, broadband) with increasing air pressure. To investigate emission line intensity variation with pressure, maximum intensity as a function of pressure for atomic, broadband, and molecular spectral features is studied and results are given in Figure 8 for (a) brass and (b) U. We find the maximum intensity of Cu I increases with increasing pressure up to the maximum pressure used in our studies (700 Torr). Broadband emission is much lower in comparison to atomic emission and only increases slightly at higher pressures. For the case of U plasma

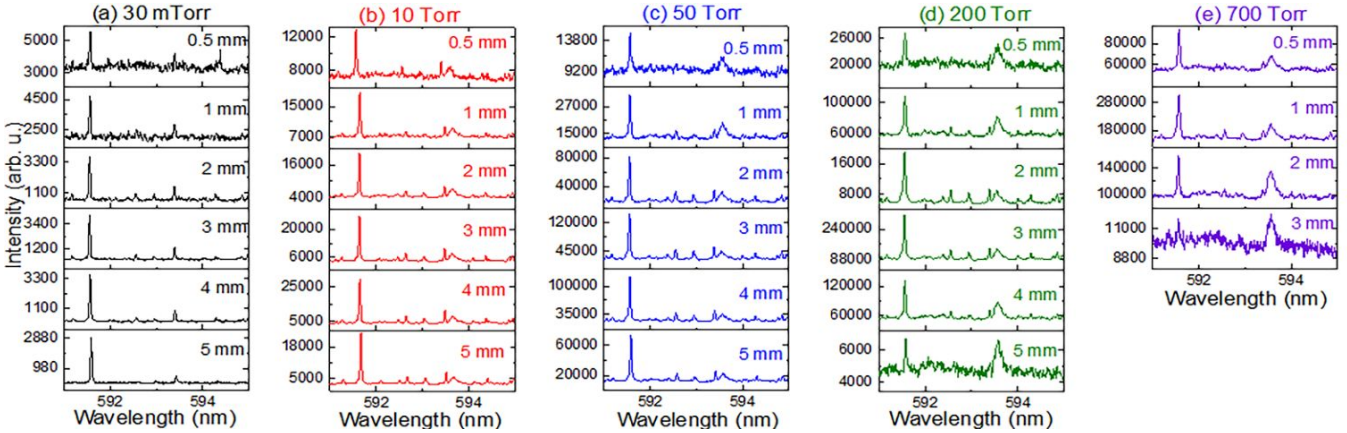

Fig. 7 Time-integrated, spatially-resolved spectral features of U plasma in the 591-595 nm wavelength range at the following pressure levels: (a) 30 mTorr, (b) 10 Torr, (c) 50 Torr, (d) 200 Torr, and (e) 700 Torr. All spectra are the average of 15 shots, and intensities are averaged over a 0.2 mm width region corresponding to the highest intensity region from the 2D spectral image. The gate delay and width used for this measurement were 1 μs and 20 μs, respectively.

emission, UO and broadband maximum emission intensities increase with increasing pressure. However, due to the presence of plasma chemistry, U I intensity peaks at ~ 200 Torr, and decreases at higher pressures, which may be due to increased gas-plasma interactions leading to the formation of UO and higher oxides. UO intensity is found to increase up to ~200 Torr, after which the rate of increase in UO emission intensity decreases, whereas broadband intensity continues increasing at higher pressures. This trend suggests that at ≥200 Torr, the presence of higher oxides (U_xO_y) is more prominent.

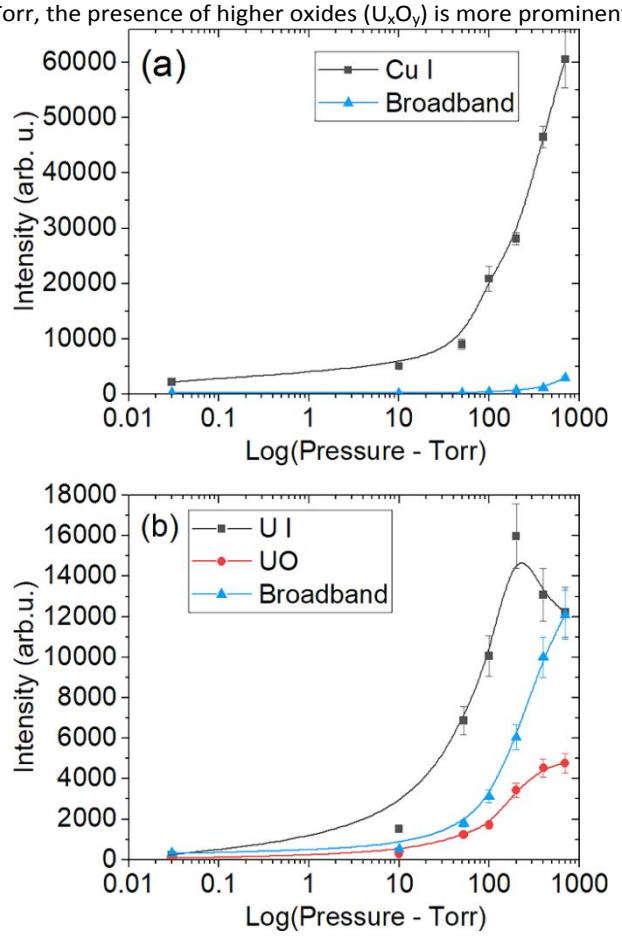

Fig. 8 Maximum intensity versus pressure (log scale) for (a) Cu I (510.55 nm) and broadband, and (b) U I (591.54 nm), UO (593.55 nm), and broadband. Intensity-pressure profiles for Cu I, U I, and UO are corrected for broadband emission. Solid lines are provided as a guide for the eye.

We also evaluated the role of plasma chemistry on the signal to background ratio (SBR) for both Cu and U atomic species. Comparing U and brass plasmas, the ambient air increases the background radiation in U plasmas by generating UO and U_xO_y. Figure 9 (a)-(b) presents SBR for atomic Cu I (510.55 nm) and U I (591.54 nm), respectively, as a function of pressure. SBRs were calculated from the maximum intensity divided by background for time-integrated emission from 1-21 µs after plasma onset. The spatial position within the plume, therefore, varied with pressure. SBR for both Cu I and U I increase from vacuum level to moderate pressure levels (~50-100 Torr), then decrease as the pressure is increased up to 700 Torr. Both plasmas showed the optimal SBR ~50-100 Torr pressure levels although the SBR values are significantly better for Cu I in brass plasmas. The increased broadband emission due to the presence of U_xO_y contributes to this decrease in SBR for U plasmas.

Changes in emission intensity and SBR ratios may be attributed both to confinement effects (illustrated via 2D spectral images and intensity-distance plots) and associated plasma oxidation for U. The plume fundamental properties such as temperature and density will also be affected by the changes in ambient pressure changes. In addition to these phenomena, the ablation mechanism will be transformed from focused fs LA to filament ablation when the ambient pressure is increased

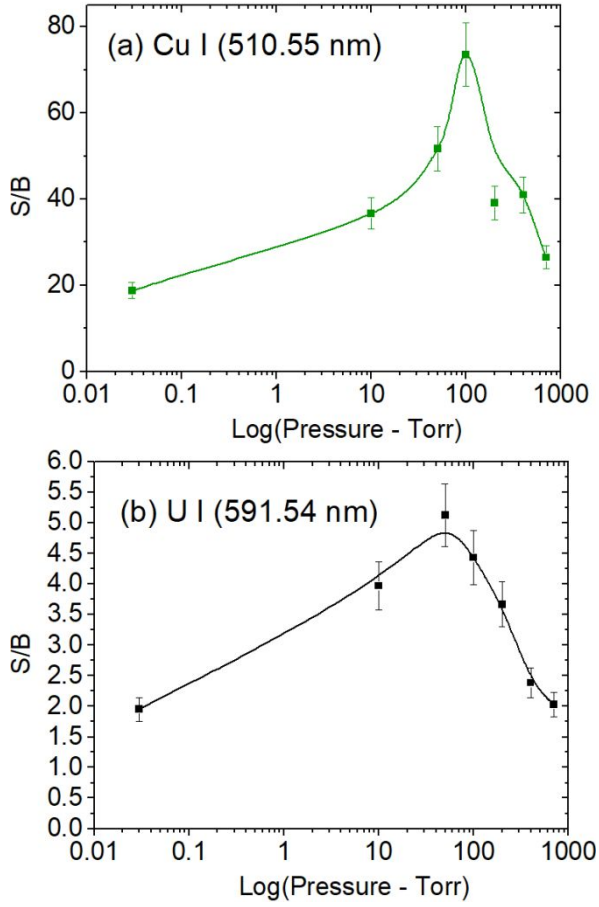

Fig. 9 Signal to background ratio for Cu I (510.55 nm) and U I (591.54 nm) as a function of pressure from 30 mTorr to 700 Torr air. Measurements were performed for time-integrated data from 1-21 µs after plasma onset, and are calculated from the maximum intensity of atomic line emission, and background signals. Solid lines are provided as a guide for the eye.

from lower-pressure levels to atmospheric conditions. Hence, we measured the excitation temperature and electron density as a function of pressure for brass plasmas whose spectroscopic constants are readily available in the literature[47] (compared to U), with results given in Figure 10.

Temperature measurements were made by assuming local thermodynamic equilibrium (LTE). Boltzmann plots were prepared using several Cu I lines (427.51, 465.11, 510.55, 515.32, 521.82, 570.03, and 578.21 nm) for measuring the excitation temperature. For electron density measurements, Stark broadening of Zn I transition at 481.05 nm was used whose electron impact width parameter was readily available in the literature.[51] More details about the temperature and density measurements can be found elsewhere.[52] Both

temperature and density measurements were taken in a space-integrated manner with an integration time of 100 ns and a delay of ~230 ns after plasma onset for all pressure levels.

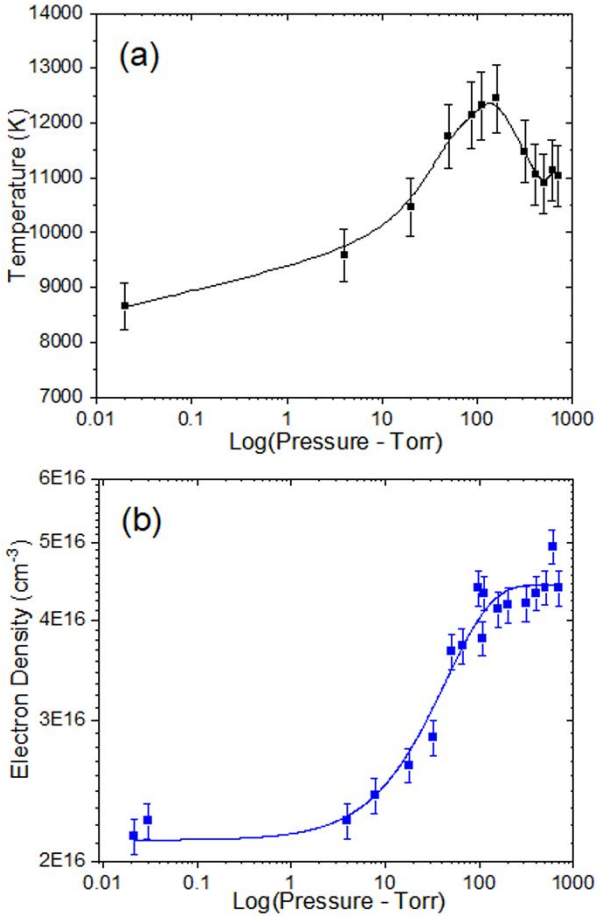

Fig. 10 (a) Excitation temperature as a function of ambient pressure for brass plasma. (b) Electron density as a function of pressure at a gate delay of 230 ns, and gate width of 100 ns. Boltzmann plots using several Cu I transitions were used for measuring excitation temperature under LTE assumption and Stark broadened profile of Zn transition was used for measuring density. The measurements were carried out in a space integrated manner.

At lower pressure levels, the estimated excitation temperature of the fs LPP brass plasma is found to be ~8,500 K. At 100 Torr, excitation temperature increases to ~12,000 K. At higher pressures (>100 Torr), a decrease in temperature with increasing pressure was evident. The electron density also showed enhancement with pressure, which can be correlated to plume confinement. For example, the measured density increased from $3x10^{16}cm^{-3}$ at 30 mTorr to $4.5x10^{16}cm^{-3}$ at 700 Torr. Measured temperature changes as a function of pressure follow changes in signal intensity for brass and U targets from low-pressure levels to 100 Torr pressure. However, it has to be mentioned that the results presented in Figure 10 are time and spatially integrated and hence the temperature and electron density measurements given in Figure 10 should be considered as average physical conditions in the plasma. It is also noted here that trends in excitation temperature and electron density reported in Figure 10 cannot be attributed to changes in ablation mechanisms (focused *versus* filament) due to several interrelated mechanisms (such as confinement) happening concurrently with increasing background pressure.

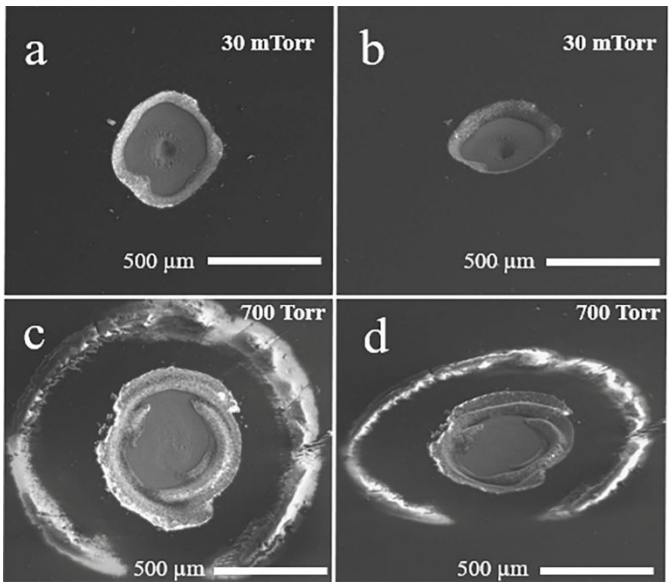

Fig. 11 Micrographs of craters generated at (a,b) 30 mTorr and (c,d) 700 Torr air for 100 shots. Images were all taken using a secondary electron detector, where images in (b) and (d) were taken at a stage tile of 52° to illustrate crater depth and morphology. The same experimental set-up and focusing conditions used for LA-OES were used to generate the craters shown here.

Ablation efficiency may vary for focused fs laser and filament ablation, which can be verified by evaluating ablation crater morphology. To investigate the impact of pressure and resultant laser focusing conditions on laser-target coupling, we examined ablation craters generated on a brass target after 100 pulses in 30 mTorr and 700 Torr air. SEM micrographs were collected using the secondary electron detector, which gives topographic information. The micrographs given in Figure 11 clearly illustrate crater morphology varies significantly for ablation in 30 mTorr *versus* 700 Torr air. The crater produced at 30 mTorr is ~500 µm in diameter, whereas the crater produced in 700 Torr via filament ablation appears much wider. In 700 Torr air, filament ablation crater is contributed both by the filament and surrounding energy reservoir, and imparts significantly less damage to the target surface than in focused fs LA. The entire crater generated via filament ablation is ~1 mm in diameter, with a central region ~500 µm in diameter. Micrographs given in Figure 11 were taken at varying stage tilt angles (0 and 52°) to demonstrate crater depth and morphology.

To further investigate crater morphology, higher magnification imaging of laser ablation craters at various locations was performed, with results given in Figures 12-13. In Figure 12, images of the central regions of craters formed in 30

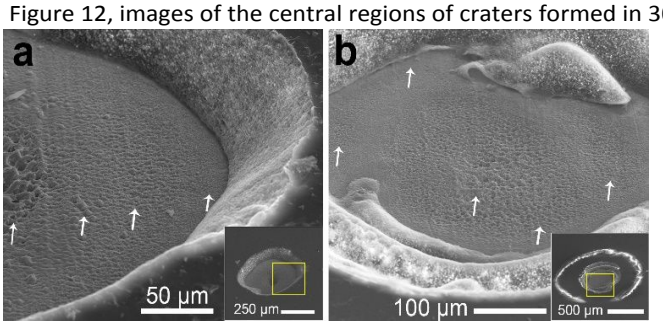

Fig. 12 Micrographs of the centre of LA craters illustrating non-uniform surface roughness for (a) 30 mTorr, 100 shots, and (b) 700 Torr air, 100 shots. The region of the ablation crater shown in the higher magnification image is indicated by a yellow box in the figure insets given in (a) and (b). White arrows indicate regions with varying surface roughness. Micrographs given above (including insets) were taken at a stage tilt of 52° degrees, using a secondary electron detector to visualize surface topology.

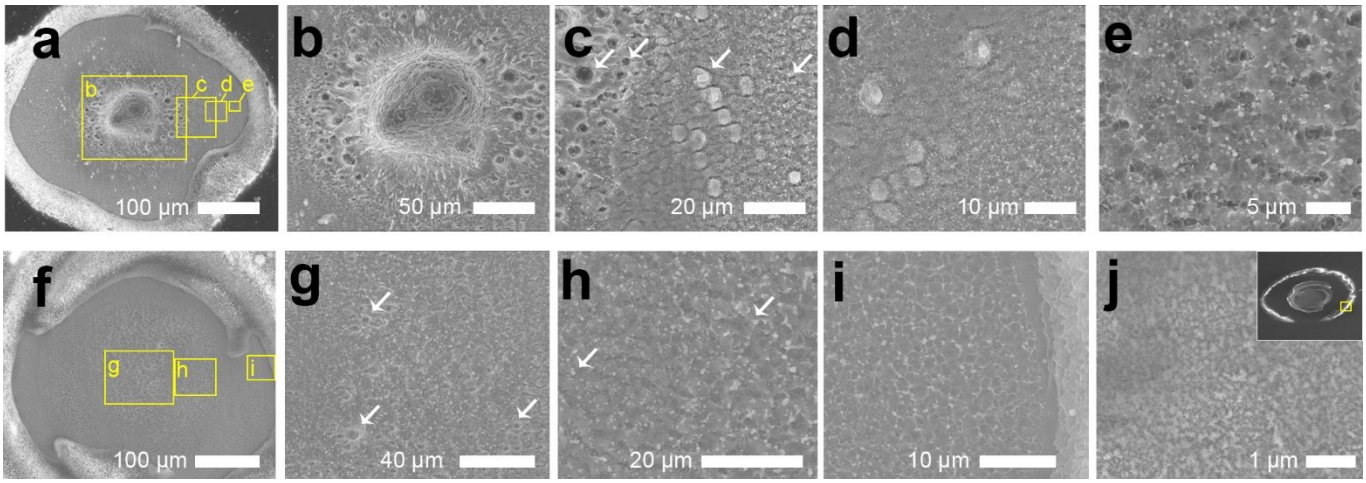

Fig. 13 Morphology of laser ablation craters generated at (a-e) 30 mTorr and (f-j) 700 Torr air for 100 shots. Low magnification images provided in (a) and (f) indicate the locations of higher magnification images with yellow boxes (not drawn to scale). Sub-figure (j) was taken from the outer region of the crater corresponding to the energy reservoir, shown as an inset. All images were all taken using a secondary electron detector at a stage tile of 0°.

mTorr and 700 Torr air illustrate varying surface roughness at different spatial locations within the crater. For the crater formed in 30 mTorr, we find roughness decreases as distance from the centre of the crater increases. However, the crater formed during filament ablation in 700 Torr air shows non-uniformly distributed regions of increased surface damage (indicated by white arrows in sub-figure b). This observation may be due to the presence of multiple filaments in the beam path.[53]

Additional micrographs of ablation crater morphologies are given in Figure 13. Low magnification images (sub-figures a and f) indicate the regions from which higher magnification images were taken for focused fs and filament ablation craters, respectively. For the focused fs LA crater, images illustrate a heterogeneous crater morphology that changes from the centre to the periphery of the crater. Evidence of particle ejection, coalescence, and agglomeration on the sample surface is evident in (b)-(e) for focused fs LA. Microscale craters/pits of varying size surround the centre fs LA crater, given in sub-figures b-c, where the material was ejected from the target. Adjacent to these pits are spherical agglomerates (sub-figure d), that were formed in the particle ejection, coalescence, and deposition processes that accompany LA. A periodic, rippled surface structure is also observed in sub-figures c-d, where ripples are ~800-900 nm in width.

Further from the central crater, smaller (nanoscale) spherical agglomerates are observed (subfigure e). A significantly different crater morphology is observed after filament ablation. The central region of the crater (sub-figures g-h) has microscale craters/pits with no evidence of significant target drilling, as seen in Figure 13(b). The filament ablation crater outer edge similarly has microscale roughness (sub-figure i). The sample surface damage from the energy reservoir is found to be less than that from filament ablation (sub-figure j).

Discussion

2D spectral imaging given in Figure 3 clearly illustrates the effect of changing ambient pressure on confinement and chemistry of brass and U plasmas. It is well known that the nature and pressure of the background medium influence the physical parameters of the plume such as densities of atoms, ions, and electrons, velocities of various plume particles and its angular distribution.[34, 54-56] Hence, the pressure of the background gas redefines the hydrodynamics of the plume regardless of the initial conditions of the plasma. The LA plumes typically expand freely without confinement effects in vacuum and in low-pressure ambient conditions. At these pressure levels, the probability of collision between the background gas species and plume species is negligible. Hence the background gas has minimal influence on the plume dynamics when the pressure increased from vacuum to low pressure levels (~10-50 mTorr). However, after a certain pressure, the plume becomes collisional with background species. This transition pressure range varies with plume conditions (pressure, temperature) as well as the target mass and nature of the ambient gas.[57] In the present experiment, ambient gas confinement effects are more pronounced at pressure levels ~ 10 Torr or higher, indicated by emission enhancement of atomic and molecular species (for the U plasma), and the movement of the stronger emitting region closer to the target (Figures 4-5).

In addition to plume expansion variation with pressure, we also observe changes in emission line intensity of atomic and molecular species (i.e. Cu I and U I, UO, and U_xO_y) from 2D spectral images (Figure 3). Since the delay and integration time used for the measurement were 1 µs and 20 µs, respectively, the contributions from continuum radiation which occurs at early times (≤ 100 ns for fs laser plasmas[58]), and from the nanoparticles which emit at later times of plume evolution[59, 60] are negligible in the Figure 3 spectral images. However, at lower ambient pressures, the collisional excitation of the plume by the ambient species is negligible and hence the weak broadband emission from nanoparticles can be seen closer to the target especially for the U plasma at ~30 mTorr. Further, emission intensities as a function of pressure for Cu I versus U species show distinctly different behaviour due to the presence of plume chemistry in the case of U. As pressure increases, confinement effects are observed for both U and brass plasmas.

However for the brass plasma, barring line intensity changes, the spectral features remain the same at different spatial locations within the plume, whereas plume chemistry influences the spectral features significantly with changing background air pressure in the U plasma.

Results from intensity-distance profiles and spatially resolved emission spectra (Figures 3 and 7, respectively) illustrate UO emission intensity increases with pressure relative to U I. Additionally, emission from U I and UO are co-located within the plume for all pressure levels over the time integration window used in this work (1-21 μs after plasma onset). Although the spatial distribution of atoms and molecules may vary with time, our prior work on U plasma expansion dynamics showed that U atoms and U monoxide are co-located within a filament produced plume for time-resolved measurements in 700 Torr air.[44] In the present study, we find that by increasing pressure from 30 mTorr to 700 Torr air, the U plume chemistry changes significantly. U atoms within the plume oxidize rapidly, where multiple reaction mechanisms of U with oxygen molecules can lead to U oxide formation (*e.g.* UO, UO_2, UO_3, U_2O_3). [25, 61] Even in low air pressure conditions, the formation of oxide molecules is possible, albeit limited due to the reduced collisions between plasma species and ambient gas. As pressure is increased, we observe an increase in emission intensity from U I, UO, and broadband (U_xO_y) spectral features. At ~100 Torr and greater pressures, U_xO_y emission dominates over UO, indicating UO is consumed in the formation of higher oxides via U atoms reacting with ambient oxygen. The increased oxide formation at higher pressure is due to increased number density of oxygen molecules as well as increased collisions between oxygen in the ambient air with plume species due to confinement.

Although changes in plasma chemistry and confinement effects are evident in 2D spectral images, further analysis of emission line intensity, SBR, plasma properties, and crater morphology was required to differentiate the role of filament *versus* focused laser pulses on emission signatures. It is well established that the nature and pressure of a background gas controls physical properties of the plasma, and thus emission line intensity and width.[27, 62] We find emission line intensity *versus* distance are distinctly different for brass and U plasmas. We can attribute this difference to the presence of U plasma chemistry, which leads to a reduction in atomic emission at higher pressures caused by the consumption of U atoms in the formation of UO and polyatomic U oxides. In contrast, the Cu I atomic emission from the brass plasma is enhanced with increasing pressure. Interestingly, the SBR for Cu I and U I emission intensities show similar trends, where SBR increases with pressure to moderate pressure levels (~50-100 Torr). Emission intensity and plasma excitation show approximately similar trends, where temperature is initially low due to free expansion at 30 mTorr, then increases with pressure due to confinement.[62] As pressure is increased further, excitation temperature decreases which we may attribute to recombination and plasma cooling, which are more significant than the heating effect caused by confinement. Although a similar trend in SBR was also observed for the U and brass plasmas, the SBR is found to be a more than an order higher for Cu analytes in brass plasma due to negligible plasma oxidation.

Comparing the emission spectroscopy signatures along with plume fundamentals, we were not able to identify the differences in ablation mechanisms or changes in plasma properties generated by focused fs pulses (~30 mTorr) and filaments (700 Torr) and this could be related to initiation of several interrelated phenomena (plasma chemistry, confinement and filament ablation) with increasing ambient pressure. However, crater morphologies highlight the significant differences in laser-target coupling between focused fs and filament ablation. The ablation crater generated via filament ablation has a larger diameter, and is shallower, indicating both filaments and energy reservoir participate in the ablation process (although the energy reservoir to a much lesser extent). In contrast, the crater produced via focused fs pulses (at 30 mTorr) had a smaller diameter, and was deeper.

Crater morphologies yield insight into ablation mechanisms and laser-target interaction. Spherical particles that appear similar to droplets are found in different sizes in the crater, where particle size decreases as distance from the centre of the crater increases. These particles were likely formed by the ejection of material from the target surface, and coalescence and agglomeration during cooling.[28, 63] This nucleation process will happen at late times in the plume lifecyle, and background gas pressure will also play a role in the nucleation of such particulates. Periodic surface structures, or ripples, are also observed in the micrographs given in Figures 12-13. Recently, modelling by Rudenko *et. al* demonstrated crater formation above the ablation threshold results in thermal ablation, leading to ripple formation in the ablation crater, which is further modified by a homogenous temperature distribution across the crater, and regulation of surface structures.[64] In our work, we find surface structure morphology varies across both fs laser and filament ablation generated craters, indicating inhomogenous energy deposition, and thus temperature distribution across the crater.

An increase in background pressure during fs laser propagation generates filaments in the laser channel, especially above certain pressure. Previous studies showed that for a fixed initial laser pulse energy, the length of the filament gets reduced with decreasing pressure.[10] This can be related to the requirement of higher critical power for self-focusing for generating filaments at lower pressures. However, the filament diameter showed an inverse relationship with pressure.[10] Hence, the probability of forming multiple filaments is reduced at lower background pressures. It has been reported that filaments are more homogeneous at lower pressures where negligible variation in filament diameter was noticed along the propagation direction.[10] However, at 30 mTorr pressure, the possibility of forming filaments is ruled out and hence the ablation mechanism can be solely due to focused fs laser pulses. Additionally, previous studies showed that the laser-target coupling will be reduced for filament ablation due to intensity clamping effects related to filament formation. [52] This concept of intensity clamping explains the shallower craters seen after filament ablation. Further, the diameter of the filament

ablation crater in our work is relatively large when compared to previously reported filament core diameters (~100 μm),[65, 66] suggesting multiple filaments are present in the beam path. This is also supported by the observation of the non-uniform distribution of surface roughness within the central crater region (Figure 12(b)) of filament ablated crater. These observations are consistent with recent work by Skrodzki *et al.*[53] Our results also show the ablation crater generated by the energy reservoir is insignificant compared to filament ablation. Filament generation conditions may also impact ablation efficiency. Previous studies showed tthat ablation efficiencies, and hence emission properties, of plasma generated by ultrafast filaments at larger distances differ significantly from laboratory scale filament generated plasmas using long focal length lenses.[52, 67] Hence, ablation properties will change with the filament generation conditions (*e.g.* strong focusing, loose focusing, or non-focusing geometry to initiate filaments in air at large stand-off distances) which in turn have a strong effect on the optical emission properties observed in LIBS.

Conclusions

In this article, we investigated the role of ambient air pressure during ultrafast laser ablation of two metallic targets with different reactivity with oxygen gas (brass and natural U). Fast-gated 2D spectral imaging was utilized over the pressure range of 30 mTorr-700 Torr air for evaluating the emission dynamics, plasma chemistry, SBR, excitation temperature, and electron density. SEM images of ablation craters formed from 100 shots at 30 mTorr and 700 Torr air pressures were also utilized for investigating differences in crater morphologies between focused fs laser *versus* filament ablation. Our results indicate that the presence of air influences the emission features of U plasma due to plasma oxidation, whereas plasma chemistry plays an insignificant role in the brass emission features. For U plasmas, the emission features at pressures ≥ 10 Torr show U atoms and UO molecules are co-located within the plume during times averaged over 1-21 μs.

Emission line intensity variation with pressure showed that U atomic and molecular spectral features exhibit different trends at higher pressure levels, indicating increased plasma oxidation leading to the formation of UO and higher oxides. This trend suggests that at pressures ≥ 200 Torr, the formation of higher oxides (U_xO_y) is more prominent than at lower pressure levels. This finding is consistent with the observed increase in broadband-like radiation present in the U plasma. SBRs are found to peak at moderate pressure levels (~50-100 Torr air) for both U and brass targets, although the SBR of Cu analytes in brass plasma is found to be one order higher than U analytes in the U plasma. Differences in emission intensity and SBR ratios between U and brass plasmas can be attributed to plasma chemistry in the U plasma. Excitation temperature was analysed for the brass plasma, and was found to vary between ~8,500K at 30 mTorr, and peak at ~12,000K at 100 Torr. Electron density was also enhanced with increasing background pressure.

Analysis of crater morphologies revealed significant differences in laser-target coupling between focused fs and filament ablation. Evidence of particulate formation, caused by material ejection, coalescence, and agglomeration during late times in plasma evolution was found in the craters formed during fs LA in 30 mTorr. Periodic, ripple surface structures were also observed, consistent with recent modelling efforts. [64] Filament ablation generated a crater with diameter of ~500 μm, and was more gentle in comparison to focused fs LA. Surface morphology varied across both fs and filament LA craters, suggesting inhomogenous energy deposition in the ablation process caused by the beam profile (in focused fs LA at lower pressures) or the presence of multiple filaments (in filament ablation at near atmospheric conditions).

By combining spatially-resolved spectral information with characterization of the plume, SBR and crater morphology analysis, a comprehensive picture of the complex interaction between plasma expansion dynamics, chemistry, properties, and differences in laser-target coupling with varying ambient pressures was obtained. It was noted that the persistence of the plasma plume and its emission varies significantly with ambient pressure. For example, the persistence of fs LPPs at low-pressure levels are limited to a couple of microseconds, however, at atmospheric pressure levels the persistence of the plume will be ~tens of microseconds.[28] Hence, the recorded features should be considered as the time-averaged conditions in the plume. The broad molecular spectral features associated with UO and U_xO_y are convoluted in the presented optical emission spectroscopy measurements due to instrumental limitations. To further explore the spectral features of UO and U_xO_y, high resolution spectroscopic tools such as laser-absorption spectroscopy and laser-induced fluorescence employing tuneable lasers[41, 68] and broadband absorption spectroscopy employing frequency combs[69] are essential.

Conflicts of interest

There are no conflicts to declare.

Acknowledgements

The authors acknowledge the U.S. Department of Energy/NNSA Office of Defense Nuclear Nonproliferation for financial support. The work presented here was performed at Pacific Northwest National Laboratory, which is operated for the U.S. DOE by Battelle Memorial Institute under Contract No. DE-AC05-76RLO1830.

References

1. S. S. Harilal, B. E. Brumfield, N. L. LaHaye, K. C. Hartig and M. C. Phillips, *Applied Physics Reviews*, 2018, **5**, 021301.
2. D. A. Cremers and L. J. Radziemski, *Handbook of laser-induced breakdown spectroscopy*, John Wiley & Sons, Chichester, West Sussex, England; Hoboken, NJ, 2013.

3. J. Wu, Y. Qiu, X. W. Li, H. Yu, Z. Zhang and A. C. Qiu, *J Phys D Appl Phys*, 2020, **53**, 023001.
4. *Laser-Induced Breakdown Spectroscopy: Theory and Applications*, Springer Heidelberg, NY, USA, 2014.
5. *Laser-induced breakdown spectroscopy*, Elsevier, Oxford, UK, 2007.
6. Q. Wang, A. Chen, Y. Wang, L. Sui, S. Li and M. Jin, *Journal of Analytical Atomic Spectrometry*, 2018, **33**, 1154-1157.
7. M. Burger, P. J. Skrodzki, J. Lin, J. Nees, K. Krushelnick and I. Jovanovic, *Opt Express*, 2018, **26**, 16456-16465.
8. L. A. Finney, P. J. Skrodzki, M. Burger, X. Xiao, J. Nees and I. Jovanovic, *Opt Express*, 2018, **26**, 29110-29122.
9. P. P. Kiran, S. Bagchi, C. L. Arnold, S. R. Krishnan, G. R. Kumar and A. Couairon, *Opt Express*, 2010, **18**, 21504-21510.
10. S. Hosseini, O. Kosareva, N. Panov, V. P. Kandidov, A. Azarm, J. F. Daigle, A. B. Savel'ev, T. J. Wang and S. L. Chin, *Laser Phys Lett*, 2012, **9**, 868-874.
11. M. Weidman, K. Lim, M. Ramme, M. Durand, M. Baudelet and M. Richardson, *Applied Physics Letters*, 2012, **101**, 034101.
12. M. Durand, A. Houard, B. Prade, A. Mysyrowicz, A. Durecu, B. Moreau, D. Fleury, O. Vasseur, H. Borchert, K. Diener, R. Schmitt, F. Theberge, M. Chateauneuf, J. F. Daigle and J. Dubois, *Opt Express*, 2013, **21**, 26836-26845.
13. S. L. Chin, *Femtosecond Laser Filamentation*, Springer-Verlag New York, 2010.
14. K. Stelmaszczyk, P. Rohwetter, G. Méjean, J. Yu, E. Salmon, J. Kasparian, R. Ackermann, J.-P. Wolf and L. Wöste, *Appl. Phys. Lett.*, 2004, **85**, 3977-3979.
15. S. Tzortzakis, D. Anglos and D. Gray, *Opt. Lett.*, 2006, **31**, 1139-1141.
16. H. M. Hou, B. Yang, X. L. Mao, V. Zorba, P. X. Ran and R. E. Russo, *Opt Express*, 2018, **26**, 13425-13435.
17. H. Kerrigan, S. R. Fairchild and M. Richardson, *Opt Lett*, 2019, **44**, 2594-2597.
18. D. W. Hahn and N. Omenetto, *Applied Spectroscopy*, 2012, **66**, 347-419.
19. D. W. Hahn and N. Omenetto, *Applied Spectroscopy*, 2010, **64**, 335a-366a.
20. S. S. Harilal, N. Farid, J. R. Freeman, P. K. Diwakar, N. L. LaHaye and A. Hassanein, *Applied Physics A*, 2014, **117**, 319-326.
21. T. A. Labutin, V. N. Lednev, A. A. Ilyin and A. M. Popov, *Journal of Analytical Atomic Spectrometry*, 2016, **31**, 90-118.
22. A. Couairon and A. Mysyrowicz, *Physics Reports*, 2007, **441**, 47-189.
23. P. Rohwetter, K. Stelmaszczyk, L. Wöste, R. Ackermann, G. Méjean, E. Salmon, J. Kasparian and J.-P. Wolf, *Spectrochim. Acta, Part B*, 2005, **60**, 1025-1033.
24. S. S. Harilal, E. J. Kautz, B. E. Bernacki, M. C. Phillips, P. Skrodzki, M. Burger and I. Jovanovic, *Physical Chemistry Chemical Physics*, 2019, **21**, 16161.
25. M. S. Finko and D. Curreli, *Phys Plasmas*, 2018, **25**, 083112.
26. M. S. Finko, D. Curreli, D. G. Weisz, J. C. Crowhurst, T. P. Rose, B. Koroglu, H. B. Radousky and M. R. Armstrong, *J Phys D Appl Phys*, 2017, **50**, 485201.
27. N. Farid, S. Harilal, H. Ding and A. Hassanein, *Journal of applied physics*, 2014, **115**, 033107.
28. P. J. Skrodzki, M. Burger, I. Jovanovic, M. C. Phillips, B. E. Brumfield, J. Yeak and S. S. Harilal, *Physics of Plasmas*, 2019, **26**, 083508.
29. P. J. Skrodzki, N. Shah, N. Taylor, K. Hartig, N. LaHaye, B. Brumfield, I. Jovanovic, M. C. Phillips and S. S. Harilal, *Spectrochimica Acta Part B-Atomic Spectroscopy*, 2016, **125** 112–119.
30. S. D. Zhang, X. H. Wang, M. H. He, Y. B. Jiang, B. C. Zhang, W. Hang and B. L. Huang, *Spectrochim Acta B*, 2014, **97**, 13-33.
31. S. Harilal, C. Bindhu, V. Nampoori and C. Vallabhan, *Applied Physics Letters*, 1998, **72**, 167-169.
32. S. S. Harilal, *Journal of Applied Physics*, 2007, **102**, 123306.
33. E. J. Kautz, P. Skrodzki, M. Burger, I. Jovanovic, B. E. Bernacki, M. C. Phillips and S. S. Harilal, *Journal of Analytical Atomic Spectrometry*, 2019, **34**, 2236-2243.
34. D. Zhang, X. Ma, S. Wang and X. Zhu, *Plasma Science and Technology*, 2015, **17**, 971-974.
35. X. L. Mao, G. C. Y. Chan, I. Choi, V. Zorba and R. E. Russo, *Journal of Radioanalytical and Nuclear Chemistry*, 2017, **312**, 121-131.
36. S. S. Harilal, B. E. Brumfield, N. Glumac and M. C. Phillips, *Optics Express*, 2018, **26**, 20319.
37. D. G. Weisz, J. C. Crowhurst, M. S. Finko, T. P. Rose, B. Koroglu, R. Trappitsch, H. B. Radousky, W. J. Siekhaus, M. R. Armstrong, B. H. Isselhardt, M. Azer and D. Curreli, *Journal of Physical Chemistry A*, 2018, **122**, 1584-1591.
38. D. G. Weisz, J. C. Crowhurst, W. J. Siekhaus, T. P. Rose, B. Koroglu, H. B. Radousky, J. M. Zaug, M. R. Armstrong, B. H. Isselhardt, M. K. Savina, M. Azer, M. S. Finko and D. Curreli, *Applied Physics Letters*, 2017, **111**, 034101.
39. P. Skrodzki, M. Burger, I. Jovanovic, B. E. Brumfield, M. C. Phillips and S. S. Harilal, *Optics Letters*, 2018, **43**, 5118.
40. K. C. Hartig, I. Ghebregziabher and I. Jovanovic, *Scientific Reports*, 2017, **7**, 43852.
41. M. C. Phillips, B. E. Brumfield, N. L. LaHaye, S. S. Harilal, K. C. Hartig and I. Jovanovic, *Scientific Reports*, 2017, **7**, 3784.
42. E. L. Gurevich and R. Hergenröder, *Applied Spectroscopy*, 2007, **61**, 233A-242A.
43. S. S. Harilal, J. Yeak, B. E. Brumfield and M. C. Phillips, *Journal of Analytical Atomic Spectrometry*, 2016, **31**, 1192-1197.
44. E. J. Kautz, J. Yeak, B. E. Bernacki, M. C. Phillips and S. S. Harilal, *Physical Chemistry Chemical Physics*, 2020, DOI: 10.1039/D0CP00078G.
45. S. S. Harilal, T. Sizyuk, A. Hassanein, D. Campos, P. Hough and V. Sizyuk, *Journal of Applied Physics*, 2011, **109**, 063306.
46. R. W. P. Pearse and A. G. Gaydon, *The identification of molecular spectra*, Chapman and Hall, London, 1976.
47. R. L. Kurucz, *R.L. Kurucz atomic linelist*, 2011, DOI: 10.17616/R3977N.
48. S. A. Irimiciuc, P.-E. Nica, M. Agop and C. Focsa, *Appl Surf Sci*, 2020, **506**, 144926.
49. K. K. Anoop, X. C. Ni, M. Bianco, D. Paparo, X. Wang, R. Bruzzese and S. Amoruso, *Appl Phys a-Mater*, 2014, **117**, 313-318.
50. P. K. Diwakar, S. S. Harilal, M. C. Phillips and A. Hassanein, *Journal of Applied Physics*, 2015, **118**, 043305.
51. M. S. Dimitrijević and S. Sahal–Bréchot, *Astronomy and Astrophysics Supplement Series*, 1999, **140**, 193-196.

52. S. S. Harilal, J. Yeak, B. E. Brumfield and M. C. Phillips, *Optics Express*, 2016, **24**, 17941.
53. P. J. Skrodzki, M. Burger and I. Jovanovic, *Scientific Reports*, 2017, **7**, 12740.
54. J. A. Aguilera and C. Aragón, *Appl. Surf. Sci.*, 2002, **197-198**, 273-280.
55. C. E. Otis, A. Gupta and B. Braren, *Applied Physics Letters*, 1993, **62**, 102-104.
56. A. V. Bulgakov and N. M. Bulgakova, *J Phys D Appl Phys*, 1998, **31**, 693-703.
57. S. S. Harilal, B. O'Shay, Y. Z. Tao and M. S. Tillack, *Journal of Applied Physics*, 2006, **99**, 083303.
58. J. R. Freeman, S. S. Harilal, P. K. Diwakar, B. Verhoff and A. Hassanein, *Spectrochimica Acta Part B-Atomic Spectroscopy*, 2013, **87**, 65-73.
59. S. Amoruso, G. Ausanio, R. Bruzzese, M. Vitiello and X. Wang, *Physical Review B*, 2005, **71**, 033406.
60. S. S. Harilal, N. Farid, A. Hassanein and V. M. Kozhevin, *Journal of Applied Physics*, 2013, **114**, 203302.
61. X.-L. Zeng, S.-Q. Huang and X.-H. Ju, *Journal of Radioanalytical and Nuclear Chemistry*, 2013, **298**, 481-484.
62. N. Farid, S. S. Harilal, H. Ding and A. Hassanein, *Applied Physics Letters*, 2013, **103**, 191112.
63. M. Kim, S. Osone, T. Kim, H. Higashi and T. Seto, *KONA Powder and Particle Journal*, 2017, **34**, 80-90.
64. A. Rudenko, C. Mauclair, F. Garrelie, R. Stoian and J.-P. Colombier, *Physical Review B*, 2019, **99**, 235412.
65. D. Kiselev, L. Woeste and J. P. Wolf, *Applied Physics B*, 2010, **100**, 515-520.
66. F. Theberge, W. W. Liu, P. T. Simard, A. Becker and S. L. Chin, *Phys Rev E*, 2006, **74**.
67. A. Valenzuela, C. Munson, A. Porwitzky, M. Weidman and M. Richardson, *Appl Phys B-Lasers O*, 2014, **116**, 485-491.
68. S. S. Harilal, C. M. Muryzn, M. C. Phillips and J. B. Martin, *Spectrochimica Acta B*, 2020, DOI: 10.1016/j.sab.2020.105828.
69. J. Bergevin, T.-H. Wu, J. Yeak, B. E. Brumfield, S. S. Harilal, M. C. Phillips and R. J. Jones, *Nature Communications*, 2018, **9**, 1273.